# Subsurface Raman Imaging with Nanoscale Resolution — **Source link** ⧉

Neil Anderson, Pascal Anger, and Achim Hartschuh, Lukas Novotny

**Institutions:** The Institute of Optics

Related papers:

- Nanoscale chemical analysis by tip-enhanced Raman spectroscopy

- High-Resolution Near-Field Raman Microscopy of Single-Walled Carbon Nanotubes

- Metallized tip amplification of near-field Raman scattering

- Nanoscale Probing of Adsorbed Species by Tip-Enhanced Raman Spectroscopy

- Probing Single Molecules and Single Nanoparticles by Surface-Enhanced Raman Scattering

Share this paper: 👤 🐦 in ✉

View more about this paper here: https://typeset.io/papers/subsurface-raman-imaging-with-nanoscale-resolution-4ldt4b52p6

# Subsurface Raman Imaging with Nanoscale Resolution

**Neil Anderson,[†] Pascal Anger,[†] Achim Hartschuh,[‡] and Lukas Novotny*,[†]**

*The Institute of Optics, University of Rochester, Rochester, New York 14627, and Institute of Physical and Theoretical Chemistry, University of Tuebingen, Tuebingen, Germany*

**ABSTRACT**

**We report on chemically specific, subsurface imaging with high spatial resolution. Using tip-enhanced Raman spectroscopy, we probe carbon nanotubes buried beneath a host dielectric media. We demonstrate our ability to map and resolve specific vibrational modes with 30 nm spatial resolution for dielectric layers with different thicknesses.**

The development of techniques that permit the structural characterization of buried nanoscale features in a nondestructive way are central for the understanding of biological processes (e.g., cell signaling, protein folding, and gene expression) and for the characterization of solid-state devices whose functional units are usually protected from interactions with the environment (capping layers). The characterization of nanoscale subsurface features poses a metrology challenge for the microelectronics industry as feature densities rise exponentially.[1] The ability to access and characterize buried nanostructures holds great promise in applications such as detecting dopants and defect sites in silicon chips[2] and imaging and manipulating hydrogen atoms buried beneath Pd[111] surfaces.[3] Recently it was shown that objects buried within a host medium could be imaged with subwavelength resolution using scanning near-field ultrasound holography (SNFUH).[4] Although SNFUH can detect localized nanostructures buried beneath surfaces with high precision, it provides no chemically specific information on the structures being imaged and relies on *prior* information of the system studied. The same is true for other high-resolution imaging techniques such as transmission electron microscopy (TEM).

As trends toward miniaturization continue to develop, so must methods and techniques that can reliably perform chemically specific characterization on the nanoscale. Recently it was shown that scattering-type near-field optical microscopy can be employed to detect gold nanostructures buried in a polymer matrix.[5] The key requirements of any technique able to successfully address these central issues are as follows: (1) nondestructive, (2) chemically specific (spectroscopy), and (3) provide spatial resolution (micros-

copy) below current silicon chip dimensions (i.e., <100 nm). One technique that satisfies all three requirements is near-field Raman spectroscopy. While the spatial resolution of traditional light microscopy is limited by diffraction to roughly $\lambda/3$,[6] the resolution of near-field microscopy is not limited by the wavelength of light. Near-field microscopy makes use of the concept of optical antennas to localize optical radiation to a spot much smaller than the diffraction limit of light. The localized spot is then raster scanned over a sample surface and an optical signature (e.g., fluorescence, Raman scattering, ...) is acquired for each image pixel. By use of a laser-irradiated metal tip as a local antenna, resolutions of $\sim\lambda/60$ have been demonstrated in combination with Raman scattering.[7]

Tip-enhanced Raman spectroscopy has revealed important new findings in our understanding of both carbon nanotubes and single molecules adsorbed to metal surfaces.[8−10] More recently, tip-enhanced Raman microscopy has been used to resolve local defect sites and study photoluminescence emission from single-walled carbon nanotubes (SWNTs) with a spatial resolution of 15 nm.[11−13] Tip-enhanced Raman imaging relies on the creation of an enhanced electric field at the apex of a sharp metal tip under laser illumination. An enhanced field is readily produced at the tip apex if the polarization of the electric field vector of the incident light is aligned along the tip shaft.[14] In this way we are able to locally excite an optical response from the sample under investigation. Here, we show that the localized field penetrates beneath the surface of the sample and allows us to image and spectrally analyze buried structures such as carbon nanotubes. In this article we describe the fabrication of test samples, outline our experimental approach, and present subsurface Raman images and spectra with a spatial resolution of 30 nm. By mapping several vibrational modes

* Corresponding author. E-mail: novotny@optics.rochester.edu.
† University of Rochester.
‡ University of Tuebingen.

characteristic of carbon nanotubes,[15] we demonstrate the ability to acquire detailed chemical maps that provide important structural information. Our experimental study is backed by rigorous electromagnetic field calculations based on the multiple multipole (MMP) method.[16]

Our experimental setup is based on an inverted optical microscope with an $x,y$ scan stage for raster scanning a sample. A laser beam ($\lambda = 633$ nm, 300 $\mu$W) is reflected by a dichroic beam splitter (BS) (10% reflection) and focused on the sample surface using a high numerical aperture microscope objective (1.4 NA). A sharp gold tip (20−30 nm diameter) is positioned in the focus of the beam and held at a constant height of 2 nm above the sample by means of a shear-force feedback mechanism.[17] A near-field Raman image is recorded by raster-scanning the sample while continuously recording the Raman scattered light. The latter is collected by the same microscope objective, transmitted by the dichroic BS, and detected either by a combination of band-pass filters and a single-photon counting avalanche photodiode (APD) or by a spectrograph equipped with a charged coupled device (CCD) cooled to −124 °C. Sharp gold tips with a radius of 20−30 nm are produced by electrochemical etching in hydrochloric acid (HCl). To establish a strong field enhancement at the tip apex in our on-axis illumination scheme, we couple the tip to the longitudinal field that is created in a tightly focused Gaussian beam.[18]

Subsurface samples used in this study are based on overcoating carbon nanotubes with a dielectric layer and were fabricated by two separate processes. The first type of sample makes use of nanosphere lithography to produce a Fischer pattern[19] of $SiO_2$ deposited on a microscope coverslip with dispersed carbon nanotubes. The fabrication of dielectric islands enables us to address both coated and uncoated sections of the same carbon nanotube. However, the deposition of $SiO_2$ on top of the nanotubes causes the surface to "warp" and hence the surface is not topography-free; i.e., the underlying nanotubes are visible in a topographic atomic force microscopy (AFM) map. This problem was overcome by fabricating a second type of sample shown schematically in Figure 1a. The fabrication process that was used is outlined as follows: (1) a thin layer (5−10 nm) of silicon dioxide ($SiO_2$) was deposited onto a piece of atomically flat mica using electron beam evaporation; (2) carbon nanotubes were spin cast from solution at 3000 rpm on top of the silicon dioxide layer; (3) an additional layer (100 nm) of silicon dioxide was then evaporated on top of the dispersed carbon nanotubes producing a carbon nanotube−dielectric sandwich; (4) the layer of $SiO_2$ was then attached to a glass microscope coverslip using an optically transparent adhesive; and (5) the thin layer of mica was then removed by soaking the entire substrate in a solution of tetrahydrofuran (THF). The substrate was then dried and flipped over before being placed onto our optical microscope; see Figure 1b.

To understand the electromagnetic response of our sample and to assess the field enhancement required to probe buried structures, we theoretically analyzed the configuration shown in Figure 1b. The calculated electromagnetic field distribution
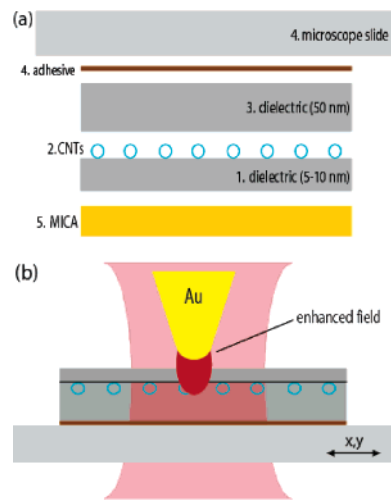


**Figure 1.** Sample geometry detailing both the fabrication process and experimental arrangement. (a) Schematic detailing the steps involved in fabricating our second sample type. (Please see main text for a full description of the fabrication process.) (b) Experimental arrangement including the presence of a sharp gold tip with an enhanced light field at the tip apex.

($|\mathbf{E}(\mathbf{r},\omega)|^2$) for a laser-irradiated gold tip placed above an $SiO_2$ substrate is shown in Figure 2a. The calculation was performed using a combination of angular spectrum and multiple multipole (MMP) methods.[20] The field distribution is represented by contour lines of constant $|\mathbf{E}(\mathbf{r},\omega)|^2$. We use a logarithmic scaling (factor of 2 between successive contour lines) in order to visualize the field over a broad range of field strengths. It is evident that the field is strongly localized and enhanced at the tip apex. The distance between adjacent contour lines increases with distance from the tip's surface, indicating that the field strength decays slower than exponentially. Because of the finite skin depth of gold, the field penetrates through the metal tip. Near the gold tip, the field vectors are predominantly normal to the tip's surface and, consequently, they are also normal to the surface of the $SiO_2$ substrate. At the $SiO_2$ surface the normal field component ($E_z$) is discontinuous because of the standard boundary condition $E_{z,\text{vac}}\epsilon_{\text{vac}} = E_{z,\text{SiO}_2}\epsilon_{\text{SiO}_2}$ with $\epsilon$ being the dielectric constant. The subscripts "vac" and "$SiO_2$" indicate the region in which the field and dielectric constant are evaluated. Therefore, the field strength $|\mathbf{E}(\mathbf{r},\omega)|^2$ underneath the $SiO_2$ layer is a factor $|\epsilon_{\text{SiO}_2}/\epsilon_{\text{vac}}|^2 \sim 5$ weaker than the field strength directly above the surface. Figure 2b shows the field strength along the $z$ axis (tip axis) for a tip−surface separation of 10 nm. At a distance of 10 nm underneath the $SiO_2$ surface, the field strength is $\sim$1000 weaker than at the tip's surface. However, most of the field drop is not associated with the discontinuity at the $SiO_2$ surface but with the tip−surface separation.

In our experiment we operate at a typical separation of 1−2 nm and the field drop is accordingly reduced. Nevertheless, because of their larger separation from the tip and because of the field discontinuity at the sample surface, buried structures experience a much weaker excitation field. Consequently, the signal-to-noise ratio (SNR) in subsurface imaging will be worse than the SNR in surface imaging. This

**Figure 2.** Calculated field distribution ($|\mathbf{E}(\mathbf{r},\omega)|^2$) near a laser-irradiated gold tip (20 nm diameter) located above a $SiO_2$ substrate. (a) Contour lines of constant $|\mathbf{E}(\mathbf{r},\omega)|^2$, factor of 2 between successive lines. (b) $|\mathbf{E}(\mathbf{r},\omega)|^2$ evaluated along the tip axis showing the discontinuous drop at the $SiO_2$ surface. The excitation field for subsurface structures is much weaker than the excitation field for surface features.

poses a significant challenge for chemically specific subsurface imaging, and it requires metal tips with high field enhancement factors. Alternatively, the field decay can be reduced by using tips with larger apex diameters, but this is at the expense of spatial resolution. Similar theoretical studies based on finite element (FE) models of tip-enhanced Raman spectroscopy using gold tips have been performed where Raman enhancements on the order of $10^5$ were estimated for dielectric layers 4 nm thick[21] and is consistent with our own findings.

This theoretical analysis helped us to identify the key challenges to be overcome in subsurface imaging. We therefore selected tips with larger tip diameters ($\sim$30 nm) and used those that exhibited particularly strong field enhancement. In Figure 3 we show the first subsurface near-field Raman images. The larger scale topographic image shown in Figure 3a reveals an $SiO_2$ Fischer pattern ($\sim$10 nm thickness) that was deposited on a glass coverslip with separated carbon nanotubes. A patterned $SiO_2$ layer is used to study the transition region between covered and uncovered nanotubes and allows us to compare directly the effects of the dielectric spacer layer on the optical resolution attainable using our tip-enhanced Raman technique. Parts b and c of Figure 3 show two sets of simultaneously acquired data: a topographic AFM image of a carbon nanotube that is partially covered by $SiO_2$ and the corresponding near-field Raman image (1590 cm$^{-1}$). The latter is composed of two distinct contributions: (1) a far-field (confocal) signal originating from the irradiation of the sample by the focused laser beam and (2) a near-field signal due to the enhanced field at the tip apex. The far-field interaction gives rise to a diffraction-limited halo whereas the near-field interaction superimposes a high-resolution image on top of the halo. As will be discussed later, near-field and far-field contributions can be

**Figure 3.** Subsurface near-field Raman imaging of carbon nanotubes overcoated with an $SiO_2$ Fischer pattern ($\sim$10 nm thickness). (a) Larger scale topographic (AFM) image of the sample revealing nanotubes that are only partially covered. (b) Topographic image of a partially over coated carbon nanotube. (c) Simultaneously acquired near-field Raman image. The contrast in the image reflects the local intensity of the Raman G band (1590 cm$^{-1}$). (d) Cross sections taken along the lines indicated in (c). The far-field background has been subtracted. Spatial resolution and signal intensity are weaker for the covered portions of the nanotube.

easily separated either experimentally during measurement or at a later stage by image processing (Fourier filtering).

The most evident (optical) feature present in the near-field Raman image (Figure 3c) is the loss of spatial resolution for the buried section of the nanotube and is readily understood in terms of the increased distance between the probe field and the sample in the presence of the dielectric layer, i.e., the field confinement becomes weaker as the
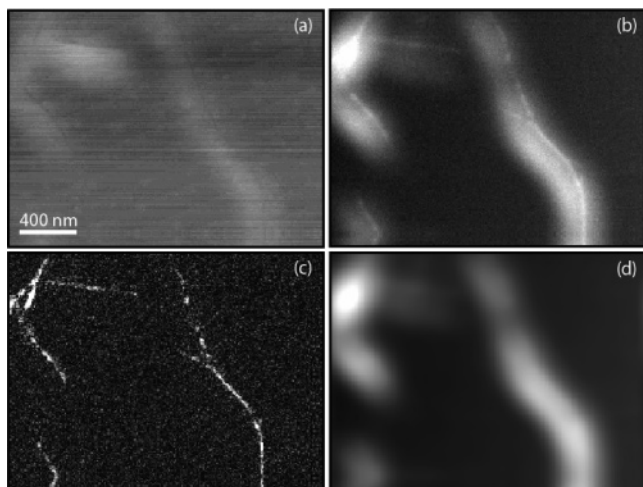
**Figure 4.** Subsurface near-field Raman imaging of carbon nanotubes overcoated with a uniform $SiO_2$ layer ($\sim$7 nm thickness): (a) topographic (AFM) image (root mean square = 0.2 nm); (b) tip-enhanced Raman ($\nu = 1590$ cm$^{-1}$) image revealing a network of carbon nanotubes buried beneath a layer of $SiO_2$; (c) near-field contribution extracted from (b); (d) confocal background extracted from (b). The near-field image reveals that Raman scattering is localized and not equally distributed along the nanotube network. The spatial resolution is $\sim$30 nm.

distance to the source is increased.[7,22] To analyze the spatial resolution more quantitatively, we subtract the far-field contribution from the signal and then evaluate the resulting near-field signal along the two lines indicated in Figure 3c. The corresponding curves are shown in Figure 3d. The near-field Raman signal from the covered portion of the nanotube is a factor of 3.2 weaker than the signal from the uncovered portion, consistent with previous theoretical predictions. Evaluation of the full widths at half-maximum (fwhm) renders the values of 28 nm for the uncovered portion of the nanotube and 64 nm for the covered portion of the nanotube. The decrease in resolution originates from the fact that the fields of a localized source spread out with distance, i.e., the field confinement becomes weaker as the distance to the source is increased. However, this set of results demonstrates that near-field Raman imaging of subsurface structures is feasible.

While nanosphere lithography allowed us to generate structured layers and to study partially overcoated tubes the technique causes uneven topographic variations as can be seen in Figure 3b. Therefore, we adopted the procedure depicted in Figure 1 to fabricate "topography-free" samples.

Figure 4 shows a data set acquired from a "topography-free" sample containing a dispersion of small carbon nanotube bundles. The data set includes: topographic image (Figure 4a), tip-enhanced Raman (1590 cm$^{-1}$) image (Figure 4b), and the decomposition of the latter into a pure near-field image (Figure 4c) and a pure far-field image (Figure 4d). The topographic map reveals that the presence of the carbon nanotubes causes the $SiO_2$ layer to "warp" rendering small bumps of height 1–2 nm and width of several hundred nanometers on the surface. (As a cross-check we performed similar AFM measurements over the same dielectric layer but without the presence of carbon nanotubes and found no

evidence of any surface "warping".) The overall root mean square variation in the topographic image is $\sim$0.2 nm.

As mentioned before in the context of Figure 3, we observe a halo in our tip-enhanced Raman images. This halo corresponds to a confocal background image and originates from the direct irradiation of the sample with the focused laser beam and wraps around the true near-field image. Retracting the tip from the sample surface makes the near-field signal disappear but not the confocal background signal. The background can obscure subwavelength details if the near-field signal is weak. To remove this image artifact, one can either apply image processing (e.g., Fourier filtering) or implement a tip modulation technique[23] to subtract the tip-up signal from the tip-down signal for every image pixel. In parts c and d of Figure 4, we have applied simple Fourier filtering to separate the near-field image from the confocal background. A disadvantage of this postprocessing approach is that most of the measurement noise is superimposed only to the near-field image and not to the confocal background image. Nevertheless, what is most evident from background subtraction are localized regions along single nanotubes where no near-field signal is generated. This localization of Raman modes is greatly obscured in the recorded Raman image (Figure 4b) and cannot be resolved by standard confocal Raman microscopy. We believe these regions have their origin in our sample preparation process, in particular the sonication method to disperse the nanotubes and to produce isolated SWNTs. Comparing our data with similar, previous SWNT studies, we believe we are imaging networks of small carbon nanotube bundles (height 3–5 nm) interconnected by individual SWNTs which yield no detectable Raman scattering. From Figure 4c the optical resolution was determined to be $\sim$30 nm. In general, we have found that using gold wire that is annealed prior to electrochemical etching provides better field enhancement and thus allows us to use sharper tips that yield higher spatial resolution (factor of 2) compared to tips fabricated from standard gold wire.

Varying the deposition conditions of the $SiO_2$ layer allowed us also to grow separated $SiO_2$ islands. We observed that some partially covered nanotubes exhibited localized phonon modes in the transition region between covered and uncovered parts. Figure 5 displays the topographic (a) and simultaneously acquired near-field Raman images over the graphite-like G′ band (2600 cm$^{-1}$) (b) and defect-induced D band (1300 cm$^{-1}$) (c), respectively. The most striking spectral feature is the localized D band scattering at the transition region located at the $SiO_2$ island–air interface. Our topographic image reveals no significant variation in the nanotube diameter nor do we observe any significant variation in G band scattering at this site. We conclude that the observed localized defect-induced scattering is a result of sidewall deformation or induced stress/strain caused by the application of the $SiO_2$ island.

Evaluating Raman scattering spectra in the presence and in absence of the gold tip reveals that the near-field enhancement is not identical for different Raman modes. On the other hand, no spectral shifts due to the localized nature

**Figure 5.** Localization of disorder-induced phonon modes. (a) Topographic image of a carbon nanotube ($\sim$2 nm diameter) partially covered by a $SiO_2$ island. (b, c) Simultaneously recorded tip-enhanced Raman images. Image (b) represents the spectral region of the G′ band ($\sim$2600 cm$^{-1}$) and image (c) the spectral region of the disorder-induced D band (1300 cm$^{-1}$). (d) Raman scattering spectra for an uncovered carbon nanotube ($\sim$2 nm diameter) resting on a glass coverslip. The spectra were recorded at the position marked in the image. The blue (green) spectrum is recorded in the presence (absence) of the gold tip. (e) Similar measurements for a buried nanotube bundle. Compared with (d) the overall Raman enhancement is weaker. The blue spectra are offset for clarity.

of the excitation source are observed. Figure 5d shows the tip-enhanced Raman image of an uncovered nanotube together with the Raman scattering spectrum evaluated at a certain location. Two spectra are shown: one in the presence of the gold tip (blue curve) and one in absence of the tip (green curve). The two spectra have the same background level with the blue curve vertically offset for clarity. While all Raman bands are enhanced when the tip is present, the enhancement factor from band to band varies. Although this effect could originate from the fact that different Raman modes have different selection rules and resonance conditions, the more likely explanation is that the confocal (tip-up) spectrum is a spatially averaged spectrum and therefore does not represent the local properties of the nanotube. Using the same gold tip, we show in Figure 5e similar measurements of a small carbon nanotube bundle covered with a 5 nm layer of $SiO_2$. The nanotube bundle is identified by two weak RBM peaks around 250 cm$^{-1}$. In comparing the spectra in parts d and e of Figure 5, we observe a noticeable decrease in Raman enhancement for the buried nanotube bundle and this result is in good agreement with the data presented in Figure 3c.

In summary, using near-field Raman scattering we have performed noninvasive, chemically specific imaging of subsurface structures with spatial resolutions down to 30 nm. Our results demonstrate the feasibility of mapping vibrational modes of carbon nanotubes that are covered with a dielectric layer. We are able to perform detailed structural analysis and relate phonon localization to defect sites in carbon nanotubes. Near-field Raman scattering also holds promise for nanoscale stress characterization in semiconductor devices. However, for most subsurface applications the near-field enhancement factor and hence the signal-to-noise ratio needs to be optimized.

**References**

(1) International Technology Roadmap for Semiconductors (http://public.itrs.net)
(2) Ippolito, S. B.; Thorne, S. A.; Eraslan, M. G.; Leblebici, Y.; Goldberg, B. B.; Unlu, M. S. *Appl. Phys. Lett.* **2004**, *84*, 4529−4531.
(3) Sykes, E. C. H.; Fernández-Torres, L. C.; Nanayakkara, S. U.; Mantooth, B. A.; Nevin, R. M.; Weiss, P. S. *Proc. Natl. Acad. Sci.,* in press.
(4) Shekhawat, G. S.; Dravid, V. P. *Science* **2005**, *310*, 89−92.
(5) Taubner, T.; Keilmann, F.; Hillenbrand, R. *Opt. Exp.* **2005**, *13*, 8893−8899.
(6) Ramsay, E.; Pleynet, N.; Xiao, D.; Warburton, R. J.; Reid, D. T. *Opt. Lett.* **2005**, *30*, 26−28.
(7) Hartschuh, A.; Sánchez, E. J.; Xie, X. S.; Novotny, L. *Phys. Rev. Lett.* **2003**, *90*, 095503.

(8) Stöckle, R. M.; Suh, Y. D.; Deckert, V.; Zenobi, R. *Chem. Phys. Lett.* **2000**, *318*, 131−136.

(9) Hayazawa, N.; Inouye, Y.; Sekkat, Z.; Kawata, S. *Chem. Phys. Lett.* **2001**, *335*, 369−374.

(10) Pettinger, B.; Ren, B.; Picardi, G.; Schuster, R.; Ertl, G. *Phys. Rev. Lett.* **2004**, *92*, 096101.

(11) Anderson, N.; Hartschuh, A.; Cronin, S. Novotny, L. *J. Am. Chem. Soc.* **2005**, *127*, 2533−2537.

(12) Anderson, N.; Hartschuh, A.; Novotny, L. *Mater. Today* **2005**, 50−54.

(13) Hartschuh, A.; Qian, H.; Meixner, A. J.; Anderson, N.; Novotny, L. *Nano Lett.* **2005**, *5*, 2310.

(14) Novotny, L.; Bian, R. X.; Xie, X. S. *Phys. Rev. Lett.* **1997**, *79*, 000645.

(15) Dresselhaus, M. S.; Dresselhaus, G.; Saito, R.; Jorio, A. *Phys. Rep.* **2005**, *409*, 47−99.

(16) Hafner, C. *The Generalized Multiple Multipole Technique for Computational Electromagnetics*; Artech: Boston, MA, 1986.

(17) Karrai, K.; Grober, R. D. *Appl. Phys. Lett.* **1995**, *66*, 1842−1844.

(18) Hartschuh, A.; Anderson, N.; Novotny, L. *J. Microsc.* **2003**, *210*, 234−240.

(19) Fischer, U. Ch.; Zingsheim, H. P. *J. Vac. Sci. Technol.* **1981**, *19*, 881−885.

(20) Novotny, L.; Hecht, B. *Principles of Nano-Optics*; Cambridge University Press: Cambridge, 2006.

(21) Notingher, I.; Elfick, A. *J. Chem. Phys. B* **2005**, *109*, 15699.

(22) Festy, F.; Demming, A.; Richards, D. *Ultramicroscopy* **2004**, *100*, 437−441.

(23) Gerton, J. M.; Wade, L. A.; Lessard, G. A.; Ma, Z.; Quake, S. R. *Phys. Rev. Lett.* **2004**, *93*, 180801.